1

Pyrocumulonimbus Events over British Columbia in 2017: An ensemble model study of parameter sensitivities and climate impacts of wildfire smoke in the stratosphere

Hsiang-He Lee[*], Katherine A. Lundquist, and Qi Tang

Lawrence Livermore National Laboratory, Livermore, CA, U.S.A.

*Corresponding author address: Dr. Hsiang-He Lee, 7000 East Avenue, Livermore, CA, 94550, U.S.A.

E-mail: lee1061@llnl.gov

Key points:

- An ensemble study of E3SM simulations determines the best combination of smoke parameters to match observations from the 2017 PyroCb events.

- The Random Forest technique is used to quantify the relative importance of parameter and finds the greatest sensitivity to injection height.

- The lifetime of stratospheric smoke from the 2017 PyroCb events is similar to the observations, about ~188 days.

Abstract

Pyrocumulonimbus (pyroCb) are fire-triggered or fire-augmented thunderstorms and can by transporting a large amount of smoke particles into the lower stratosphere. With satellite remote sensing measurements, the plumes from pyroCb events over British Columbia in 2017 were observed in the lower stratosphere for about 8-10 months after the smoke injections. Several previous studies used global climate models to investigate the physical parameters for the 2017 pyroCb events, but the conclusions show strong model dependency. In this study, we use Energy Exascale Earth System Model (E3SM) atmosphere model version 1 (EAMv1) and complete an ensemble of runs exploring three injection parameters: smoke amount, the ratio of black carbon to smoke, and injection height. Additionally, we consider the heterogeneous reaction of ozone and primary organic matter. According to the satellite daily observed aerosol optical depth, we find that the best ensemble member is the simulation with 0.4 Tg of smoke, 3% of which is black carbon, a 13.5 km smoke injection height, and a 10^{-5} probability factor of the heterogeneous reaction of ozone and primary organic matter. We use the Random Forest machine learning technique to quantify the relative importance of each parameter in accurately simulating the 2017 pyroCb events and find that the injection height is the most critical feature. Due to the long lifetime and wide transport of stratospheric aerosols, the estimated e-folding time of smoke aerosols in the stratosphere is about 188 days, and the global averaged shortwave surface cooling is -0.292 W m^{-2} for about 10 months.

Plain Language Summary

Pyrocumulonimbus (pyroCb) caused by extreme wildfires can transport a large amount of smoke particles into the lower stratosphere, which then affects the climate. Several previous studies used global climate models, along with satellite observations of smoke, to investigate the injection parameters for 2017 pyroCb events over British Columbia, but the conclusions show strong model dependency. This study uses the Energy Exascale Earth System Model (E3SM) atmosphere model version 1 (EAMv1) and completes an ensemble of simulations targeting three loosely constrained injection parameters: smoke amount, the ratio of black carbon to smoke, and injection height. Additionally, we consider the heterogeneous reaction of ozone and primary organic matter in the ensemble model. We use the Random Forest machine learning technique to quantify the importance of each parameter in accurately simulating the 2017 pyroCb event. Finally, a model simulation with the best combination of injection parameters shows the estimated smoke lifetime in the stratosphere is about 188 days, and a global-averaged shortwave surface cooling of -0.292 W m^{-2} for about 10 months.

Keywords:

1   Introduction

In recent years, extreme wildfires have frequently occurred in the western United States and Canada. Pyrocumulonimbus (pyroCb) are fire-triggered or fire-augmented thunderstorms and can transport a large amount of smoke particles into the lower stratosphere (Fromm et al., 2005; Fromm et al., 2010). Aerosols in the lower stratosphere from volcanic eruptions and large wildfires have been detected and monitored with the modern satellite remote sensing observations in the past decades (Fromm et al., 2000; Peterson et al., 2018; Vernier et al., 2009).

PyroCb and volcanic eruptions are important geophysical extreme events because they can perturb the stratospheric aerosol loading for several months and have substantial climate impacts locally and globally. The smoke aerosols injected into the stratosphere from pyroCbs mainly contain black carbon (BC) and organic carbon (OC) aerosols (Andreae, 2019; Andreae & Merlet, 2001; Park et al., 2003) and have different radiative effects from the sulfate aerosols released by volcanic eruptions. Volcanic sulfate aerosols have a strong cooling effect due to scattering. With carbonaceous aerosols, BC absorbs shortwave radiation, while particulate organic matter scatters it, which leads to atmosphere warming and surface cooling (Bergstrom et al., 2002; Malone et al., 1985). Additionally, through the absorption of solar radiation and subsequent heating, BC can self-loft, lengthening its atmospheric lifetime. In the 1980s, Malone et al. (1985) used a three-dimensional circulation model to simulate injected smoke in the atmosphere that might be introduced by a nuclear war. They concluded that the heating from BC shortwave absorption gives rise to vertical motions that carry smoke above the original injection height around the tropopause. Later, the changes of solar heating profile due to BC absorption were supported by the measurements of the field campaign, High-performance Instrumented Airborne Platform for Environmental Research Pole-to-Pole Observations (HIPPO), between early 2009 and mid-2011

95   (Schwarz et al., 2013). Thus, the radiative effects of the pyroCb injected smoke in the stratosphere

96   can be very important in the global radiation budget.

97   Several previous studies used satellite observations and global climate models (GCMs) to

98   investigate the injection parameters for 2017 pyroCb events over British Columbia, but the

99   conclusions show strong model dependency (Christian et al., 2019; Das et al., 2021; Yu et al.,

100 2019). The pyroCb events occurring in British Columbia, Canada in August 2017 were considered

101 the most extensive known stratospheric intrusion from pyroCb activity at that time. Based on the

102 combination of lidar and passive remote sensing observations, Peterson et al. (2018) estimated the

103 injected aerosol amount of 0.1-0.3 Tg, while Torres et al. (2020) projected around 0.18-0.35 Tg,

104 by using three different satellite remote sensing observations, comparable to a moderately sized

105 volcanic eruption (Ge et al., 2016; Hofmann et al., 2009; J. Wang et al., 2013). In previous studies,

106 smoke injection height varies from 10 km (Das et al., 2021) to 13 km (Christian et al., 2019; Yu

107 et al., 2019), and the ratio of BC to smoke ranges from 2% - 6%. GCM simulations in Christian

108 et al. (2019) show that the pyroCb smoke particles cause radiative forcing of 0.02 W m^{-2} at the top

109 of the atmosphere (TOA), averaged globally in the 2 months following the events; however, Das

110 et al. (2021) saw -0.03 W m^{-2} global mean radiative forcing at TOA in the first month after the

111 events. Both studies used the NASA Goddard Earth Observing System (GEOS) with a chemical

112 transport model to conduct their simulations, but the model configurations were different.

113   Wagman et al. (2020) used the Department of Energy (DOE) Energy Exascale Earth

114 System Model (E3SM) atmosphere model version 1 (EAMv1) to examine the climate impacts of

115 massive urban fires in South Asia induced by a regional nuclear exchange scenario. The study

116 found that uncertainties in the modeled aerosol radiative properties and smoke composition,

117 particularly the percentage of BC and primary organic matter (POM) in the total aerosol mass,

118   propagate through to produce significant uncertainties in the climate response. In their study,

119   overall climate impacts are comparable in initial magnitude (i.e., surface cooling), but have a much

120   a shorter duration compared to previous assessments with the same smoke injection (Mills et al.,

121   2014; Reisner et al., 2018).

122   In this study, we use EAMv1 with the CMIP6 (Coupled Model Intercomparison Project

123   Phase 6) configuration, which is different from the CMIP5 used in Wagman et al. (2020), to assess

124   the 2017 pyroCb event over British Columbia and perform an ensemble simulation targeting three

125   important, yet uncertain fire smoke injection parameters: smoke amount, the ratio of black carbon

126   to smoke, and injection height. Additionally, we consider the probability parameter (gamma) of

127   the heterogeneous reaction of ozone and organic carbon suggested by Yu et al. (2019) in the

128   ensemble experiments. The purpose of this study is to quantify the performance of the E3SM

129   model in simulating the climate disturbance of a stratospheric wildfire smoke injection, when

130   compared to observations. We also want to examine the lifetime of stratospheric smoke in EAMv1,

131   and the magnitude and duration of the climate perturbation, to see if they agree with observations,

132   as this would have important implications for studies of climate impacts due to a nuclear exchange,

133   for example Wagman et al. (2020).

134   A brief description of EAMv1, simulation set-up, parameters for the ensemble study, and

135   observational data are given in Section 2. Simulation results and discussion are shown in Section

136   3 and Section 4, respectively, with a summary provided in Section 5.

137 ## 2   Methodology

138 ### 2.1   Model description and configuration

139   The DOE E3SM coupled model version 1 was released to the community in April 2018.

140   A detailed description is documented in Golaz et al. (2019). The overview of the atmosphere

141   component of E3SMv1, E3SM Atmosphere Model (EAMv1) is provided by Rasch et al. (2019).

142   EAMv1 uses a spectral element dynamical core at a 110-km resolution (at equator) on a cubed

143   sphere geometry and a traditional hybridized sigma-pressure vertical coordinate. The transition

144   between terrain-following and constant-pressure coordinates is made at ~200 hPa (~11km).

145   EAMv1 has 72 vertical layers with a model top at approximately 60 km (10 hPa).

146   EAMv1 uses the two-moment Modal Aerosol Module (MAM4), with four internally mixed

147   lognormal size modes, to represent the size distribution and mixing state of aerosols (X. Liu et al.,

148   2016). EAMv1 has several enhanced features in MAM4 (H. Wang et al., 2020). One important

149   modification to MAM4 is that based on the original MAM3, the addition of freshly emitted primary

150   carbonaceous aerosols (e.g., BC and POM) as a primary-carbon mode to treat the aging process of

151   BC/POM, when combined with the three commonly defined size aerosol modes (Aitken,

152   accumulation, and coarse mode). The transfer or "aging" of carbonaceous aerosols from the

153   primary-carbon mode to the accumulation mode occurs after particles condense eight monolayers

154   of (hydrophilic) sulfate, particles condense enough secondary organic aerosol (SOA) to change the

155   volume-weighted hygroscopicity by the same amount as eight layers of sulfate, or particles

156   coagulate with hydrophilic Aitken-mode particles.

157   The stratospheric ozone is simulated by the linearized chemistry version 2 (Linoz v2) (Hsu

158   & Prather, 2009), which calculates the first-order Taylor expansion terms for the stratospheric

159   ozone production and loss based on local temperature, local ozone abundance, and the overhead

160   ozone column.

161   In this study, we choose the compset F2010C5-CMIP6-LR, which configures an

162   atmosphere-only simulation using the CMIP6 forcing and prescribed sea surface temperature and

163   sea ice with observed climatology. The initial condition of the model configuration is from an

164   E3SMv1 Atmospheric Model Intercomparison Project (AMIP) simulation (Golaz et al., 2019) on

165   January 1, 2010. Monthly climatological emissions from 2005 to 2014 are used to generate

166   background aerosols in the atmosphere. The default EAMv1 CMIP6 setup uses climatological

167   volcanic aerosols' optical properties to calculate aerosol radiative effects in the stratosphere

168   instead of explicitly calculating existing aerosol radiative effects, which are function of aerosol

169   particle size and concentration. To study the impacts of the 2017 cyroCb event, we removed the

170   CMIP6 pre-calculated volcanic aerosol radiative effects and added wildfire smoke as an extra

171   aerosol source in the stratosphere. Note that in this study, the instantaneous radiative effects of

172   stratospheric aerosols are diagnosed by performing two sets of radiative transfer calculations (i.e.,

173   double call), one with stratospheric aerosols only and the other without any aerosols in the model

174   column, to calculate the flux differences.

175   2.2   Nudging for meteorological conditions

176   Nudging is a method of data assimilation to constrain the evolution of the prognostic

177   variables to be similar to the evolution of those variables in a predefined reference simulation (e.g.,

178   reanalysis data). In general, only a small number of model variables are nudged, and other fields

179   are allowed to evolve in response to the physical and dynamical processes in the model.

180   In order to provide more realistic meteorological conditions to facilitate the time-specific

181   evaluations of fire simulations against observations, we nudge towards ERA-Interim data, which

182   is a global atmospheric reanalysis from the European Centre for Medium-Range Weather

183   Forecasts (ECMWF) (*ERA-Interim Project*, 2009) and provides 6-hourly U and V wind

184   components, and temperature (T) for meteorology nudging. The simulation runs from January 1,

185   2017, to August 11, 2017, with the horizontal wind components and temperature nudged towards

186   the ERA-Interim reanalysis data, following the setup in Yu et al. (2019), and using linear function

187   nudging (Sun et al., 2019; Tang et al., 2019) with a 50-hourly time frequency (i.e., relaxation time

188   scale). Starting from August 12, 2017, the day of the PyroCb event, the model runs freely without

189   nudging to the end of May of 2018 to simulate smoke transport and aerosol-radiation interactions.

190   The evaluation and discussion of the nudging time scale are in Section 3.1.

191   2.3   Numerical experiments for the ensemble study

192   Previous studies demonstrated that three injection parameters: total smoke amount, the

193   ratio of black carbon to smoke, and injection height are critical for accurate simulation of the

194   smoke transport (Christian et al., 2019; Das et al., 2021; Yu et al., 2019). Additionally, Yu et al.

195   (2019) highlighted the importance of the effective reaction probability (i.e., gamma number) of

196   heterogenous reaction between ozone and primary organic matter (POM) in simulating

197   stratospheric fire smoke lifetime.

198   The heterogeneous reaction of ozone and POM is not included in the standard EAMv1

199   release. In this study, the rate of the heterogeneous reaction (molecules cm^{-3} s^{-1}) is given by the

200   following:

201                              $$R = \frac{1}{4}\gamma v_A A_p n_A, \quad (1)$$

202   where g is the probability of the reaction, which is a perturbed parameter in the ensemble; v_A is

203   the mean speed of ozone (cm s^{-1}); A_p is the total surface area of POM per unit volume of air (cm^2

204   cm^{-3}); n_A is the gas-phase concentration of ozone (molecules cm^{-3}) (Seinfeld & Pandis, 2012). We

205   assume that the ozone mixing ratio in the stratosphere will not be affected after the reaction, but

206   the POM concentration will decrease based on the reaction rate (Yu et al., 2019).

207   Running an ensemble of simulations with different parameter values can help determine

208   the parameter setting for minimizing differences between simulations and observations. Our

209   approach is to use an ensemble with four varied, or perturbed, parameters to determine the

11

210   parameter values which, when used in an E3SM simulation, produce the best fit to observations

211   and equally importantly to quantify the model sensitivities to these parameters. We additionally

212   use our ensemble to examine uncertainty within the E3SM simulations (Anderson & Lucas, 2018;

213   Murphy et al., 2004), and would like to highlight that such an ensemble perturbation experiment

214   has not been done for the 2017 pyroCb study before.

215   In this study, we run 144 simulations with varied values listed in Table 1. We add smoke

216   at a variable injection height near 52°N, 120°W, where the 2017 pyroCb event was observed from

217   the satellite remote sensing. The perturbed smoke amount and BC ratio is injected on a continuous

218   basis for 5 hours from 19 UTC to 23 UTC on August 12, 2017. The injected smoke aerosols only

219   contain BC and POM, which are added to the primary-carbon mode in MAM4. In addition to

220   injecting an aerosol mass of BC and POM, the number concentration is also calculated based on

221   the volume mean diameter (0.134 mm) and the BC/POM density (1.8/1.4 g cm^{-3}) (Liu et al., 2012).

222   Each ensemble member is given a name based on the value of four parameters. For

223   example, 0.2Tg_BC2_12km_gamma6 means the simulation with 0.2 Tg smoke, of which 2% is

224   BC, a 12 km smoke injection height, and a gamma number of 10^{-6} in the heterogeneous reaction

225   calculation.   We also run a control simulation (CNTL) without a smoke injection or a

226   heterogeneous reaction applied to the POM.

227   2.4   Observations and the "ensemble score"

228   The Stratospheric Aerosol and Gas Experiment III (SAGE-III) is mounted on the

229   International Space Station (ISS). SAGE-III Version 5.1 data from the instrument are available

230   from June 2017, and level 2 data are used in this study. SAGE-III uses solar and lunar occultation

231   and limb scatter to infer profiles of trace gases like ozone and aerosol extinction coefficient at nine

232   wavelengths between 384 and 1544 nm. We choose to use the aerosol extinction coefficient at

233   1024 nm for most analyses in this study, which also follows the analysis in Yu et al. (2019).

234   SAGE-III provides a nearly direct extinction measurement in its occultation mode, but the

235   occultation measurement provides generally poor spatial coverage. The measurements only occur

236   during the orbital sunrise and sunset. Thus, SAGE-III acquires 30 sets of profiles per day in two

237   latitudes bands that roughly span 60°N to 60°S over a month. Details of SAGE-III ISS

238   measurements are documented in Cisewski et al. (2014).

239   We use the SAGE-III aerosol extinction coefficient to derive daily aerosol optical depth

240   (AOD) integrated from 16 km to 20 km as the reference. Then, we compute daily AOD for each

241   ensemble member to calculate the correlation and the mean square error (MSE) between modeled

242   AOD and satellite retrieved AOD. Based on the correlation and MSE among all ensemble

243   members, we can calculate an "ensemble score" for each member, which is defined as follows:

244        $ensemble\ score = -normalized(MSE) + normalized(correlation)$ (2)

245   Normalized MSE and normalized correlation will get a number range from 0 to 1. A perfect

246   ensemble case gets 1 as the highest ensemble score, which means MSE is zero and correlation gets

247   1 between modeled AOD and satellite retrieved AOD. Based on the ensemble scores, we can

248   evaluate the model performance of an individual simulation, each with a unique combination of

249   ensemble parameters.

250   2.5   Machine learning technique – Random Forest

251   Machine learning is now being used to quantify the performance of multi-model climate

252   ensemble members (Monteleoni et al., 2011), determine the sensitivity of climate models to

253   parameter values and resolution (Anderson & Lucas, 2018), and detect features in large climate

254   data sets (Y. Liu et al., 2016). In this study, we apply a supervised machine learning technique,

255   known as random forest (Breiman, 2001) to a perturbed smoke injection parameter ensemble of

256   EAMv1 simulations. We use the *feature importance* function in the scikit-learn random forest

257   package (Pedregosa et al., 2011) to measure the importance of each feature. The function takes an

258   array of features and computes the normalized total reduction of the criterion brought by that

259   feature. In other words, features with high scores strongly partition the data and lie near the parent

260   node in a decision tree. By perturbing the values of features in a tree and monitoring the fits'

261   accuracy, each feature's importance is estimated. The highest score is the most important feature

262   in the forecasting machine.

263   A group of randomized decision trees on different bootstrap samples of the training data is

264   important to add a further level of randomness to splitting the trees. The scikit-learn random forest

265   package we use in the study provides 50 trees, an internal bootstrap option, including the

266   calculation of validation scores, and default settings for other fitting parameters. Furthermore, we

267   also test the use of 10 or 100 decision trees for the training data to increase the variation of random

268   forests. The train/test split varies from 70%/30% to 90%/10% with a 5% interval.

269   3   Results and discussions

270   3.1   Model evaluation of meteorological nudging

271   The relaxation time scale of nudging applied in global climate models is 6 hours in many

272   previous studies, basically focusing on the tropospheric studies (Kooperman et al., 2012; Sun et

273   al., 2019; Telford et al., 2008), but use of this relaxation time scale can strongly disturb the

274   background aerosols in the stratosphere. Thus, we want to see how different nudging time scales

275   affect EAMv1 results and, to the best of our knowledge, no EAMv1 papers have documented it.

276   In a set of sensitivity tests of nudging U, V and T with different relaxation time scales, ranging

277   from 6 to 50 hours, we find that while a shorter relaxation time scale can better constrain the

278   meteorological fields toward the ERA-Interim reanalysis data, the differences within this range are

279   minor (figures not shown). However, a more significant issue, seldom mentioned in most studies,

280   is that the background aerosol in the stratosphere becomes unrealistically high and deviates

281   significantly from the control simulation without nudging.

282   Figure 1a shows the time series of area-averaged smoke mass mixing ratio (kg Tg-air^{-1}) in

283   CNTL without meteorological nudging applied. The smoke aerosol mixing ratio above 15 km

284   height is less than 0.1 kg Tg-air^{-1}, and the aerosol mixing ratio in the stratosphere should not be

285   disturbed much by surface emissions, especially in the absence of extreme wildfire events or

286   volcanic eruptions. However, once we apply the meteorological nudging with a 6-hour relaxation

287   time scale, tropospheric aerosols are transported upward to the stratosphere, and accumulate with

288   time due to the lack of wet scavenging at high altitudes (Figure 1b). Davis et al. (2022) suggested

289   that a 12- to 24-hour nudging time scale is appropriate for minimizing errors; however, in our case,

290   even with a relaxation time scale of 24 hours, the issue is not solved (Figure 1c). They also tried

291   a 48-hour nudging time scale to eliminate the errors in the background and spatial patterns of

292   constituents but at the cost of losing fidelity in the nudged variables. Because the purpose of

293   nudging in this study is only to constrain synoptic variability, we use a 50-hour relaxation time

294   scale to get stable stratospheric background aerosols (Figure 1d) without sacrificing too much

295   accuracy of the nudged meteorological fields.

296   3.2   Ensemble runs and sensitivity to perturbed parameters

297   Examining the ensemble score (Eq. 2) for every ensemble member, we find the highest

298   score is 0.85, achieved with the parameters set to 0.4 Tg of smoke, of which 3% is BC, with an

299   injection height of 13.5 km, and a gamma value of 10^{-5} (named 0.4Tg_BC3_13.5km_gamma5).

300   Time series of daily AOD integrated from 16 to 20 km in altitude is shown in Figure 2 from August

301   13, 2017, to May 31, 2018. This ensemble member captures the timing and value of AOD

302 reasonably, as compared to the SAGE-III observations. The peak AOD from SAGE-III occurs in

303 early September at about 0.002. The ensemble member 0.4Tg_BC3_13.5km_gamma5 also

304 captures the value and timing of the peak in the daily AOD compared to SAGE-III. After

305 September, the AOD decay rate in 0.4Tg_BC3_13.5km_gamma5 compares well with the satellite

306 retrieved AOD from SAGE-III, but slightly slow. Thus, the model simulates higher AOD till late

307 January 2018. After late January 2018, the modeled AOD matches well the satellite retrieved

308 AOD again till in early May 2018.

309 In order to illustrate how sensitive the model is to each perturbed parameter, Figure 3 shows

310 the boxplot of daily AOD of the member with the highest ensemble score (i.e.,

311 0.4Tg_BC3_13.5km_gamma5) compared with the other ensemble members when each parameter

312 is independently varied. Because AOD is derived directly from the smoke amount, the

313 distinguishable AOD differences among the ensemble members with various smoke amounts are

314 clearly shown in Figure 3a. On the other hand, the AOD in the other two perturbed parameter

315 comparisons, BC ratio and injection height, are more challenging to differentiate (Figures 3b –

316 3c). Figure 3d shows the important role of heterogenous reaction rate on smoke aerosol decay in

317 the stratosphere. Overall, Figure 3 shows a common approach for the model intercomparison, but

318 it could mislead one to conclude the model is more sensitive to smoke amount or gamma number.

319 Figure 4 shows the boxplot and the mean ensemble score for four perturbed parameters.

320 The mean ensemble score, for example, increases with smoke amount from -0.12 in the group of

321 0.2 Tg to 0.38 in the group of 0.4 Tg (Figure 4a). The mean ensemble score for simulations with

322 varied BC ratio shows a similar trend, increasing with increased BC ratio, from -0.09 in the 1%

323 BC group to 0.45 in the 5% BC group. Interestingly, when the injection height is varied, the

324 highest mean ensemble score is 0.44 and occurs in the group with a 13.5 km injection height, while

16

325   the lowest mean score is -0.22 in the group with a 12 km injection height. This shows that the

326   mean ensemble score changes significantly with different smoke injection heights. In other words,

327   the model is more sensitive to the change of smoke injection height than to the other perturbed

328   parameters. On the other hand, the mean ensemble score of the cases with a gamma number of

329   10^{-5}, 10^{-6}, and 10^{-7} are 0.20, 0.19, and 0.17, respectively. The ensemble score is similar across

330   variation in the gamma number, meaning that the model shows little sensitivity to the choice of

331   gamma number.

332   The *feature importance* function in the scikit-learn random forest package also calculates

333   that injection height is the most important feature in this study with a score of 0.42, followed by

334   smoke amount (0.30), BC ratio (0.23), and gamma number (0.05) (Figure 5). This result is

335   consistent with what we show in Figure 4 – the larger variance of the mean ensemble scores, the

336   more important feature is in the model.

337   3.3   Smoke transport and altitude

338   The 2017 pyroCb event was observed by the Cloud-Aerosol Lidar and Infrared Pathfinder

339   Satellite Observation (CALIPSO) satellite, and the plume height was about 13.5 km on August 14

340   (Figure 5 in Das et al., 2021). At this altitude, the smoke is above the tropopause, and westerlies

341   dominate the smoke transport. In our simulation, the smoke is transported to the East coast of the

342   U.S. about 4 to 5 days after the fire smoke is injected (Figure 6b), and within 10 days, the smoke

343   reaches most European countries (Figure 6d).

344   We notice that as the smoke aerosols approach Hudson Bay in eastern Canada, the smoke

345   is transported southward due to the jet stream (Figure 6b). Once the smoke moves to the lower

346   midlatitudes (~45°N) and rises to a height of ~18 km, the dominant winds change from westerlies

347   to easterlies, so the smoke transport turns westward (Figure 6c-d). Therefore, this pyroCb event

348   has two transport paths in the stratosphere, and the smoke aerosols rapidly spread over the entire

349   midlatitude area within three weeks after the smoke is injected (Figure 6e). In late September

350   2017, the fire smoke aerosols cover almost the entire northern hemisphere (Figure 6f).

351   　　Our result shows that plume rise height is important to the plume transport and smoke

352   aerosol concentration in the lower stratosphere. Based on the definition of maximum plume height

353   in Thomason et al. (2018), where the aerosol extinction coefficient is greater than 1.5×10^{-4} km^{-1},

354   50% higher than the background value in the lower stratosphere, our simulated maximum plume

355   rise height in 0.4Tg_BC3_13.5km_gamma5 matches the plume rise height observed by SAGE-III

356   well (Figure 7). The initial rise of the modeled plume occurs at a rate of 0.25 km day^{-1}, attaining

357   heights of 20 km in late September. It is noted here that once the smoke aerosol is injected into

358   the stratosphere, the plume rise does not rely only on vertical motions within the atmosphere, but

359   also on heating of the black carbon through absorption of shortwave solar radiation (Yu et al.,

360   2019). Heating of the black carbon is considered in EAMv1, but the internal mixing state of

361   aerosols in MAM4 does not perfectly represent the core-shell structure of BC with other chemical

362   species.

363   3.4   Smoke lifetime and radiative effects

364   　　As discussed earlier, Wagman et al. (2020) used an older EAMv1 configuration to examine

365   the climate impacts of mass urban fires in South Asia induced by a regional nuclear exchange

366   scenario. Their study showed a shorter smoke lifetime in the stratosphere than in other similar

367   studies, which is one motivation for the work here. In this work, our calculation for the 2017

368   pyroCb smoke lifetime in the stratosphere reasonably matches the observations and previous

369   studies. Figure 8a shows the decay rate of EAMv1 aerosol optical depth (blue dashed line), which

370   is calculated starting from September 1, 2017. Based on this decay rate, the model gives an e-

371   folding time of ~188 days, while on the same starting day, an e-folding time of 227 days is

372   calculated from SAGE-III data. The estimated e-folding time only changes by one or two days in

373   either EAMv1 or SAGE-III when the decay period starts from mid-September, which is the peak

374   of AOD. This suggests little sensitivity to the starting date.

375   Yu et al. (2019) reported that the lifetime of the stratospheric smoke was observed to be

376   ~150 days for the 2017 pyroCb events. We use another quantity, the smoke column mass

377   (BC+POM) concentration, to calculate an e-folding time of ~137 days, which is close to the

378   observations from SAGE-III depicted in Yu et al. (2019) (Figure 8b). Das et al. (2021), also

379   reported an e-folding time of ~140-150 days from their results running the Goddard Earth

380   Observing System (GEOS) atmospheric general circulation model (AGCM) and the also from

381   OMPS-LP (Ozone Mapping Profiler Suite Limb Profiler) observations. Our study and Yu et al.

382   (2019) considered the heterogeneous reaction between organics present in the smoke and ozone in

383   the stratosphere, which plays a role in matching the observed decay. By contrast, in Das et al.

384   (2021) and Christian et al. (2019), this heterogeneous reaction is not considered, and the pyroCb

385   smoke lifetime is simply the dynamical lifetime of the smoke in the model, which includes the

386   removal by large scale circulations, aerosol sedimentation, and aerosol radiative heating/cooling.

387   Due to the long lifetime and wide transport of stratospheric aerosols, the pyroCb injected

388   stratospheric smoke can affect the global radiative budget. Figure 9a shows the spatial-temporal

389   averaged radiative effects of simulated smoke aerosols over the northern hemisphere from August

390   13, 2017, to May 31, 2018. The main impact of the stratospheric smoke aerosols is shortwave

391   surface cooling, which has an averaged value of -0.292 W m^{-2}. The absorption of solar radiation

392   also causes warming in the atmosphere by 0.515 W m^{-2}. Since the longwave radiative effects of

393 stratospheric aerosols are minor, the net radiative effects of smoke aerosols are close to the

394 shortwave values (Figure 9a).

395   The radiative effects of smoke aerosols are small in the long-term average. However, the

396 pyroCb aerosols have strong atmospheric warming and surface cooling effects for about 2-3

397 months after the smoke injections (Figure 9b and 9c). The atmospheric warming and surface

398 cooling are most pronounced between 30 - 80°N, consistent with Das et al. (2021). The maximum

399 values of the net radiative effect occur within the first 7-10 days after the smoke injections, causing

400 atmospheric warming up to 5.21 W m^{-2} and a surface cooling of about -5.83 W m^{-2}. Our calculated

401 radiative effects in Figure 9b and 9c are similar to the results presented in Das et al. (2021), which

402 found that the pyroCb smoke particles result in a maximum radiative warming of 8.3 W m^{-2} in the

403 atmosphere and radiative cooling of -5.4 W m^{-2} at the surface. It is noted that their results are all-

404 sky radiative effects, but Figure 9 are clear-sky radiative effects.

4   Discussion

406   Figure 2 shows that our simulated AOD from the best ensemble case,

407 0.4Tg_BC3_13.5km_gamma5, matches the derived AOD from SAGE-III well. However, we

408 notice that the modeled extinctions are overestimated in the lower stratosphere, in comparison to

409 the observations (Figure 10a). The modeled smoke extinctions are much higher than the

410 extinctions from SAGE-III at the beginning of the injection. Once the modeled extinctions reach

411 the peak at 16 km height, the rate of the modeled smoke extinction declines slower than the

412 observed rate. By contrast, the model underestimates the extinction coefficient at the altitude of

413 20 km (Figure 10c). The modeled extinctions match the observed extinctions well in the first few

414 weeks after the injection, even background stratospheric aerosol extinction at the beginning of the

415   pyroCb events. However, the descending rate of the modeled extinction is faster than the observed

416   extinction, especially at a height of 20 km.

417   In Das et al. (2021), the modeled result also has a negative bias at higher altitudes (> 20

418   km) and a positive bias at lower altitudes, especially for the first 10-20 days after the smoke

419   injection. Based on their explanation, there are two reasons - the modeled background

420   stratospheric aerosol extinctions are lower than OMPS-LP retrievals at the higher levels (a negative

421   bias at higher altitudes), and the modeled smoke plumes are lower than the observed plumes, which

422   reached as high as 22 km (a positive bias at lower altitudes). In our simulation, the modeled

423   background aerosol extinctions are comparable with SAGE-III. The main reason for the biases of

424   modeled extinctions could be a combination of errors in the smoke self-lofting and coarse vertical

425   resolution at these altitudes.

426   As we mentioned in Section 3.3, the self-lofting of smoke aerosols comes from heating of

427   the black carbon, which is included in EAMv1, but the internal mixing state of aerosols in MAM4

428   does not perfectly represent the core-shell structure of BC with other chemical species. The mixing

429   state of aerosols affects aerosol growth and radiative forcing. Thus, the model is not sensitive to

430   changes in the BC ratio and does not generate strong vertical motions from the heating of the black

431   carbon. The other possible reason is the coarse vertical resolution. EAMv1 has a traditional

432   hybridized sigma pressure vertical coordinate. The vertical resolution in the stratosphere in

433   EAMv1 is about 450 – 800 m, which is much coarser than the resolution in the lower troposphere

434   (dz = ~100 m). Regardless of if the vertical motion of the smoke aerosols is caused by dynamics

435   or thermal buoyancy, the coarse vertical resolution cannot represent the vertical transport properly.

436   The coarse vertical resolution could be one reason why, although the smoke aerosols are injected

437   at the correct height, aerosols descend at different rates in the lower and higher stratosphere (Figure

438   10).

5   Summary

440   We use EAMv1 to reexamine the 2017 pyroCb events over British Columbia and complete

441   an ensemble of runs targeting three uncertain injection parameters: smoke amount, the ratio of

442   black carbon to the smoke amount, and injection height. We also consider the probability

443   parameter of the heterogeneous reaction of ozone and organic carbon suggested by Yu et al.

444   (2019). According to the daily aerosol optical depth (AOD) integrated from 16 km to 20 km,

445   derived from the SAGE-III aerosol extinction coefficient at 1024 nm wavelength, we define an

446   "ensemble score" for each member and get a highest score of 0.85 achieved by the ensemble

447   member 0.4Tg_BC3_13.5km_gamma5,which has 0.4 Tg of smoke , 3% of which is BC, a 13.5

448   km smoke injection height, and 10^{-5} gamma number in the heterogeneous reaction.

449   The case of 0.4Tg_BC3_13.5km_gamma5 captures the time of the peak in AOD and also

450   the decay rate, as compared to the satellite retrieved AOD from SAGE-III. We examine model

451   sensitivity to different values of each perturbed parameter (i.e., smoke amount, the ratio of black

452   carbon to smoke, injection height, and gamma number), and the results show that the model is

453   more sensitive to a change in smoke injection height and less sensitive to variation in the gamma

454   number. This conclusion is supported by the *feature importance* function in the scikit-learn

455   random forest package. The injection height is the most important feature in this study, with a

456   score of 0.42, followed by smoke amount (0.30), BC ratio (0.23), and gamma number (0.05).

457   The pyroCb smoke aerosols simulated in this study have two main transport paths in the

458   stratosphere. The smoke aerosols rapidly spread throughout the entire midlatitude area within

459   three weeks after the smoke is injected and cover almost the entire northern hemisphere for about

460   50 days. Our calculation for the 2017 pyroCb smoke lifetime in the stratosphere reasonably

461   matches the observations and previous studies. Based on the decay rate of daily AOD, the model

462   gives an e-folding time of 188 days, while SAGE-III suggests an e-folding time of 227 days. We

463   use another quantity, the smoke column mass (BC+POM) concentration, to calculate an e-folding

464   time at different level heights, and our estimated e-folding time is close to the observations from

465   SAGE-III, about 137 days.

466   Due to the long lifetime and wide transport of stratospheric aerosols, the radiative effects

467   of the pyroCb injected smoke in the stratosphere can be important in the global radiation budget.

468   The pyroCb aerosols have strong atmospheric warming and surface cooling effects for about 2-3

469   months after the smoke injection. The atmospheric warming and surface cooling are most

470   pronounced between 30 - 80°N. Averaging the entire simulation period, the major impact of

471   stratospheric aerosols is the shortwave surface cooling, which has a spatiotemporal averaged value

472   of -0.292 W m^{-2} over the north hemisphere from August 13, 2017, to May 31, 2018. The shortwave

473   radiative effects of stratospheric aerosols also cause warming in the atmosphere by 0.515 W m^{-2}.

474   Our simulated AOD from the best ensemble member, 0.4Tg_BC3_13.5km_gamma5,

475   matches the derived AOD from SAGE-III well. However, the modeled aerosol extinctions have a

476   negative bias at the higher altitudes (~ 20 km) and a positive bias lower in the stratosphere (~16

477   km). The combination of the internal mixing state of aerosols in MAM4 and the coarse vertical

478   resolution in the stratosphere could cause the model to lack fidelity in simulating smoke aerosol

479   self-lofting and vertical motions. Thus, further studies are needed to get a realistic aerosol mixing

480   structure in MAM4 and a higher vertical resolution in the stratosphere.

481

482   **Code and data availability:**

483   The model code used in this study is located at https://doi.org/10.5281/zenodo.6383271.   The

484   extinction   coefficient   simulated   by   EAMv1   can   be   found   at

485   https://doi.org/10.5281/zenodo.6476400.   Other EAMv1 simulated outputs are available upon

486   request from Hsiang-He Lee (lee1061@llnl.gov).

487

Acknowledgements:

496

Reference

498   Anderson, G. J., & Lucas, D. D. (2018). Machine Learning Predictions of a Multiresolution
499   Climate Model Ensemble. *Geophysical Research Letters, 45*(9), 4273-4280.
500   doi:https://doi.org/10.1029/2018GL077049
501   Andreae, M. O. (2019). Emission of trace gases and aerosols from biomass burning – an updated
502   assessment. *Atmos. Chem. Phys., 19*(13), 8523-8546. doi:10.5194/acp-19-8523-2019
503   Andreae, M. O., & Merlet, P. (2001). Emission of trace gases and aerosols from biomass burning.
504   *Global   Biogeochemical   Cycles,   15*(4),   955-966.
505   doi:https://doi.org/10.1029/2000GB001382
506   Bergstrom, R. W., Russell, P. B., & Hignett, P. (2002). Wavelength Dependence of the Absorption
507   of Black Carbon Particles: Predictions and Results from the TARFOX Experiment and
508   Implications for the Aerosol Single Scattering Albedo. *Journal of the Atmospheric
509   Sciences, 59*(3), 567-577. doi:10.1175/1520-0469(2002)059<0567:Wdotao>2.0.Co;2
510   Breiman, L. (2001). Random forests. *Machine learning, 45*(1), 5-32.

Christian, K., Wang, J., Ge, C., Peterson, D., Hyer, E., Yorks, J., & McGill, M. (2019). Radiative Forcing and Stratospheric Warming of Pyrocumulonimbus Smoke Aerosols: First Modeling Results With Multisensor (EPIC, CALIPSO, and CATS) Views from Space. *Geophysical Research Letters, 46*(16), 10061-10071. doi:https://doi.org/10.1029/2019GL082360

Cisewski, M., Zawodny, J., Gasbarre, J., Eckman, R., Topiwala, N., Rodriguez-Alvarez, O., . . . Hall, S. (2014). *The Stratospheric Aerosol and Gas Experiment (SAGE III) on the International Space Station (ISS) Mission* (Vol. 9241): SPIE.

Das, S., Colarco, P. R., Oman, L. D., Taha, G., & Torres, O. (2021). The long-term transport and radiative impacts of the 2017 British Columbia pyrocumulonimbus smoke aerosols in the stratosphere. *Atmos. Chem. Phys., 21*(15), 12069-12090. doi:10.5194/acp-21-12069-2021

Davis, N. A., Callaghan, P., Simpson, I. R., & Tilmes, S. (2022). Specified dynamics scheme impacts on wave-mean flow dynamics, convection, and tracer transport in CESM2 (WACCM6). *Atmos. Chem. Phys., 22*(1), 197-214. doi:10.5194/acp-22-197-2022

ERA-Interim Project. (2009). Retrieved from: https://doi.org/10.5065/D6CR5RD9

Fromm, M., Alfred, J., Hoppel, K., Hornstein, J., Bevilacqua, R., Shettle, E., . . . Stocks, B. (2000). Observations of boreal forest fire smoke in the stratosphere by POAM III, SAGE II, and lidar in 1998. *Geophysical Research Letters, 27*(9), 1407-1410. doi:https://doi.org/10.1029/1999GL011200

Fromm, M., Bevilacqua, R., Servranckx, R., Rosen, J., Thayer, J. P., Herman, J., & Larko, D. (2005). Pyro-cumulonimbus injection of smoke to the stratosphere: Observations and impact of a super blowup in northwestern Canada on 3–4 August 1998. *Journal of Geophysical Research: Atmospheres, 110*(D8). doi:https://doi.org/10.1029/2004JD005350

Fromm, M., Lindsey, D. T., Servranckx, R., Yue, G., Trickl, T., Sica, R., . . . Godin-Beekmann, S. (2010). The Untold Story of Pyrocumulonimbus. *Bulletin of the American Meteorological Society, 91*(9), 1193-1210. doi:10.1175/2010bams3004.1

Ge, C., Wang, J., Carn, S., Yang, K., Ginoux, P., & Krotkov, N. (2016). Satellite-based global volcanic SO2 emissions and sulfate direct radiative forcing during 2005–2012. *Journal of Geophysical Research: Atmospheres, 121*(7), 3446-3464. doi:https://doi.org/10.1002/2015JD023134

Golaz, J.-C., Caldwell, P. M., Van Roekel, L. P., Petersen, M. R., Tang, Q., Wolfe, J. D., . . . Zhu, Q. (2019). The DOE E3SM Coupled Model Version 1: Overview and Evaluation at Standard Resolution. *Journal of Advances in Modeling Earth Systems, 11*(7), 2089-2129. doi:10.1029/2018ms001603

Hofmann, D., Barnes, J., O'Neill, M., Trudeau, M., & Neely, R. (2009). Increase in background stratospheric aerosol observed with lidar at Mauna Loa Observatory and Boulder, Colorado. *Geophysical Research Letters, 36*(15). doi:https://doi.org/10.1029/2009GL039008

Hsu, J., & Prather, M. J. (2009). Stratospheric variability and tropospheric ozone. *Journal of Geophysical Research: Atmospheres, 114*(D6). doi:https://doi.org/10.1029/2008JD010942

Kooperman, G. J., Pritchard, M. S., Ghan, S. J., Wang, M., Somerville, R. C. J., & Russell, L. M. (2012). Constraining the influence of natural variability to improve estimates of global aerosol indirect effects in a nudged version of the Community Atmosphere Model 5. *Journal of Geophysical Research: Atmospheres, 117*(D23). doi:https://doi.org/10.1029/2012JD018588

556   Liu, X., Easter, R. C., Ghan, S. J., Zaveri, R., Rasch, P., Shi, X., . . . Mitchell, D. (2012). Toward
557   a minimal representation of aerosols in climate models: description and evaluation in the
558   Community Atmosphere Model CAM5. *Geosci. Model Dev., 5*(3), 709-739.
559   doi:10.5194/gmd-5-709-2012

560   Liu, X., Ma, P. L., Wang, H., Tilmes, S., Singh, B., Easter, R. C., . . . Rasch, P. J. (2016).
561   Description and evaluation of a new four-mode version of the Modal Aerosol Module
562   (MAM4) within version 5.3 of the Community Atmosphere Model. *Geosci. Model Dev.,*
563   *9*(2), 505-522. doi:10.5194/gmd-9-505-2016

564   Liu, Y., Racah, E., Correa, J., Khosrowshahi, A., Lavers, D., Kunkel, K., . . . Collins, W. (2016).
565   Application of deep convolutional neural networks for detecting extreme weather in
566   climate datasets. *arXiv preprint arXiv:1605.01156.*

567   Malone, R. C., Auer, L. H., Glatzmaier, G. A., Wood, M. C., & Toon, O. B. (1985). Influence of
568   Solar Heating and Precipitation Scavenging on the Simulated Lifetime of
569   Post—Nuclear War Smoke. *Science, 230*(4723), 317-319.
570   doi:doi:10.1126/science.230.4723.317

571   Mills, M. J., Toon, O. B., Lee-Taylor, J., & Robock, A. (2014). Multidecadal global cooling and
572   unprecedented ozone loss following a regional nuclear conflict. *Earth's Future, 2*(4), 161-
573   176. doi:https://doi.org/10.1002/2013EF000205

574   Monteleoni, C., Schmidt, G. A., Saroha, S., & Asplund, E. (2011). Tracking climate models.
575   *Statistical Analysis and Data Mining: The ASA Data Science Journal, 4*(4), 372-392.
576   doi:https://doi.org/10.1002/sam.10126

577   Murphy, J. M., Sexton, D. M. H., Barnett, D. N., Jones, G. S., Webb, M. J., Collins, M., &
578   Stainforth, D. A. (2004). Quantification of modelling uncertainties in a large ensemble of
579   climate change simulations. *Nature, 430*(7001), 768-772. doi:10.1038/nature02771

580   Park, R. J., Jacob, D. J., Chin, M., & Martin, R. V. (2003). Sources of carbonaceous aerosols over
581   the United States and implications for natural visibility. *Journal of Geophysical Research:*
582   *Atmospheres, 108*(D12). doi:https://doi.org/10.1029/2002JD003190

583   Pedregosa, F., Varoquaux, G., Gramfort, A., Michel, V., Thirion, B., Grisel, O., . . . Dubourg, V.
584   (2011). Scikit-learn: Machine learning in Python. *the Journal of machine Learning*
585   *research, 12*, 2825-2830.

586   Peterson, D. A., Campbell, J. R., Hyer, E. J., Fromm, M. D., Kablick, G. P., Cossuth, J. H., &
587   DeLand, M. T. (2018). Wildfire-driven thunderstorms cause a volcano-like stratospheric
588   injection of smoke. *npj Climate and Atmospheric Science, 1*(1), 30. doi:10.1038/s41612-
589   018-0039-3

590   Rasch, P. J., Xie, S., Ma, P.-L., Lin, W., Wang, H., Tang, Q., . . . Yang, Y. (2019). An Overview
591   of the Atmospheric Component of the Energy Exascale Earth System Model. *Journal of*
592   *Advances in Modeling Earth Systems, 11*(8), 2377-2411. doi:10.1029/2019ms001629

593   Reisner, J., D'Angelo, G., Koo, E., Even, W., Hecht, M., Hunke, E., . . . Cooley, J. (2018). Climate
594   Impact of a Regional Nuclear Weapons Exchange: An Improved Assessment Based On
595   Detailed Source Calculations. *Journal of Geophysical Research: Atmospheres, 123*(5),
596   2752-2772. doi:https://doi.org/10.1002/2017JD027331

597   Schwarz, J. P., Samset, B. H., Perring, A. E., Spackman, J. R., Gao, R. S., Stier, P., . . . Fahey, D.
598   W. (2013). Global-scale seasonally resolved black carbon vertical profiles over the Pacific.
599   *Geophysical Research Letters, 40*(20), 5542-5547.
600   doi:https://doi.org/10.1002/2013GL057775

601 Seinfeld, J. H., & Pandis, S. N. (2012). *Atmospheric chemistry and physics: from air pollution to*
602   *climate change* (2 ed.): Wiley.
603 Sun, J., Zhang, K., Wan, H., Ma, P.-L., Tang, Q., & Zhang, S. (2019). Impact of Nudging Strategy
604   on the Climate Representativeness and Hindcast Skill of Constrained EAMv1 Simulations.
605   *Journal of Advances in Modeling Earth Systems, 11*(12), 3911-3933.
606   doi:https://doi.org/10.1029/2019MS001831
607 Tang, Q., Klein, S. A., Xie, S., Lin, W., Golaz, J. C., Roesler, E. L., . . . Zheng, X. (2019).
608   Regionally refined test bed in E3SM atmosphere model version 1 (EAMv1) and
609   applications for high-resolution modeling. *Geosci. Model Dev., 12*(7), 2679-2706.
610   doi:10.5194/gmd-12-2679-2019
611 Telford, P. J., Braesicke, P., Morgenstern, O., & Pyle, J. A. (2008). Technical Note: Description
612   and assessment of a nudged version of the new dynamics Unified Model. *Atmos. Chem.*
613   *Phys., 8*(6), 1701-1712. doi:10.5194/acp-8-1701-2008
614 Thomason, L. W., Ernest, N., Millán, L., Rieger, L., Bourassa, A., Vernier, J. P., . . . Peter, T.
615   (2018). A global space-based stratospheric aerosol climatology: 1979–2016. *Earth Syst.*
616   *Sci. Data, 10*(1), 469-492. doi:10.5194/essd-10-469-2018
617 Torres, O., Bhartia, P. K., Taha, G., Jethva, H., Das, S., Colarco, P., . . . Ahn, C. (2020).
618   Stratospheric Injection of Massive Smoke Plume From Canadian Boreal Fires in 2017 as
619   Seen by DSCOVR-EPIC, CALIOP, and OMPS-LP Observations. *Journal of Geophysical*
620   *Research: Atmospheres,   125*(10),   e2020JD032579.
621   doi:https://doi.org/10.1029/2020JD032579
622 Vernier, J. P., Pommereau, J. P., Garnier, A., Pelon, J., Larsen, N., Nielsen, J., . . . McDermid, I.
623   S. (2009). Tropical stratospheric aerosol layer from CALIPSO lidar observations. *Journal*
624   *of   Geophysical   Research: Atmospheres,   114*(D4).
625   doi:https://doi.org/10.1029/2009JD011946
626 Wagman, B. M., Lundquist, K. A., Tang, Q., Glascoe, L. G., & Bader, D. C. (2020). Examining
627   the Climate Effects of a Regional Nuclear Weapons Exchange Using a Multiscale
628   Atmospheric Modeling Approach. *Journal of Geophysical Research: Atmospheres,*
629   *125*(24), e2020JD033056. doi:https://doi.org/10.1029/2020JD033056
630 Wang, H., Easter, R. C., Zhang, R., Ma, P.-L., Singh, B., Zhang, K., . . . Yoon, J.-H. (2020).
631   Aerosols in the E3SM Version 1: New Developments and Their Impacts on Radiative
632   Forcing. *Journal of Advances in Modeling Earth Systems, 12*(1), e2019MS001851.
633   doi:10.1029/2019ms001851
634 Wang, J., Park, S., Zeng, J., Ge, C., Yang, K., Carn, S., . . . Omar, A. H. (2013). Modeling of 2008
635   Kasatochi volcanic sulfate direct radiative forcing: assimilation of OMI SO_2
636   plume height data and comparison with MODIS and CALIOP observations. *Atmos. Chem.*
637   *Phys., 13*(4), 1895-1912. doi:10.5194/acp-13-1895-2013
638 Yu, P., Toon, O. B., Bardeen, C. G., Zhu, Y., Rosenlof, K. H., Portmann, R. W., . . . Robock, A.
639   (2019). Black carbon lofts wildfire smoke high into the stratosphere to form a persistent
640   plume. *Science, 365*(6453), 587-590. doi:10.1126/science.aax1748

641

642

643　　Table 1. The range of parameters describing the smoke injection and the gamma number of the
644　　heterogenous reaction of ozone and particulate organic matter in the ensemble runs
645

Parameter (unit)	Range
Smoke amount (Tg)	[0.2, 0.3, 0.4]
BC to smoke ratio (%)	[1, 2, 3, 5]
Injection height (km)	[12, 12.5, 13, 13.5]
Gamma number (unitless)	[10^{-7}, 10^{-6}, 10^{-5}]

646
647

648
649

650
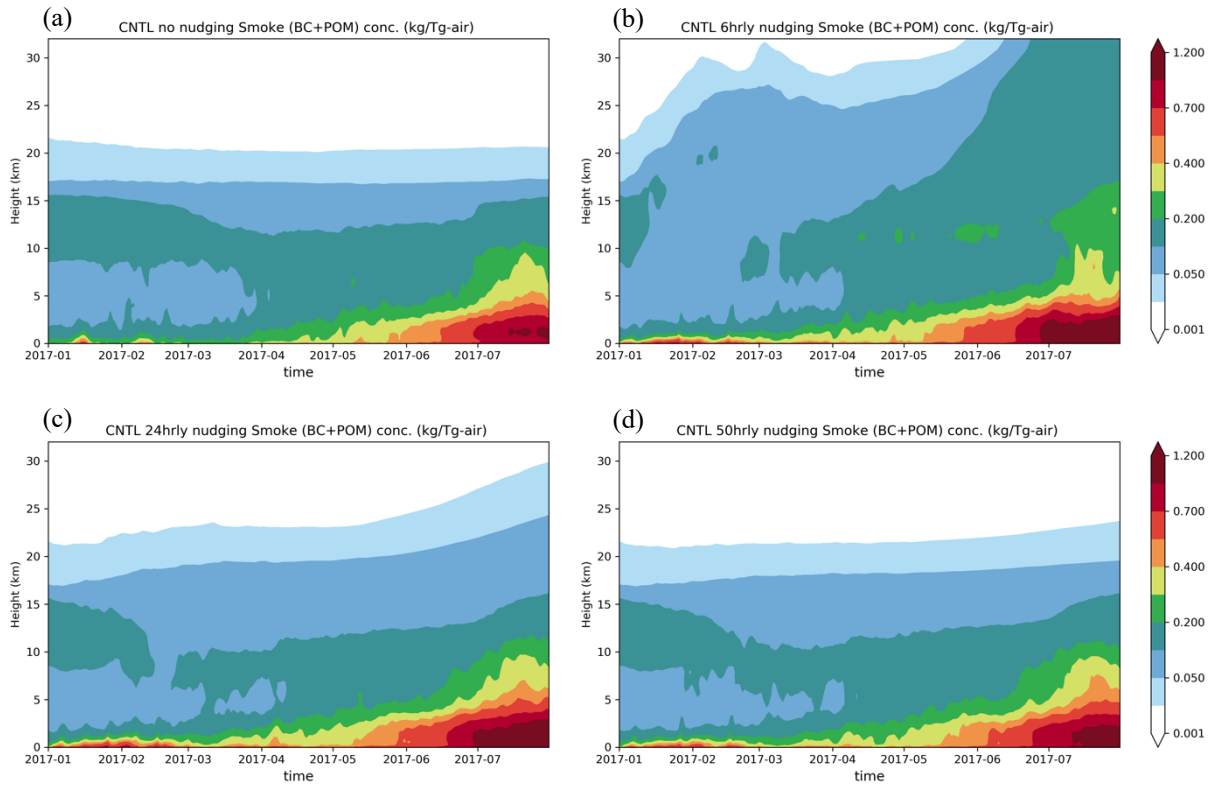
651
652 Figure 1. (a) Time series of area-averaged smoke (BC+POM) mass mixing ratio (kg Tg-air^{-1}) in
653 the control simulation (CNTL) without meteorological nudging applied. (b) – (d) The same as in
654 (a), but with the horizontal wind components and temperature nudged toward the ERA-Interim
655 reanalysis data with 6, 24, and 50-hour relaxation time scales, respectively. Area is averaged from
656 a latitude of 40°N to 80°N.

657
658

AOD from 16km to 20 km
0.4Tg_BC3_13.5km_gamma5 (score: 0.85)
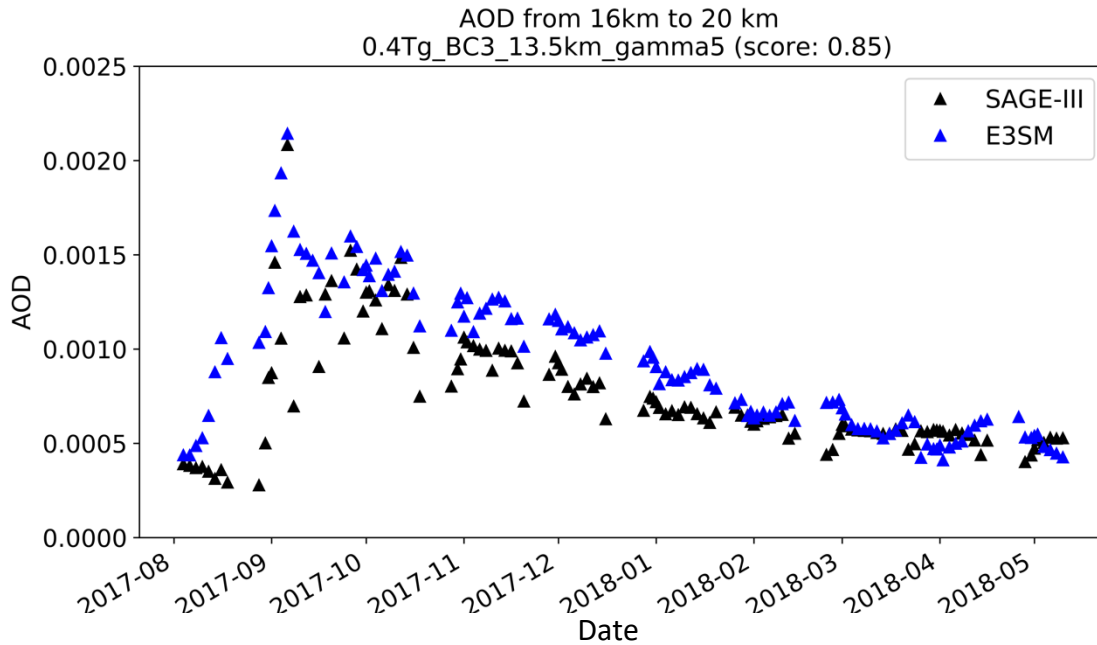
659
660
Figure 2. Time series of daily AOD (unitless) integrated from 16 km to 20 km in height. Black triangles are the derived AOD from SAGE-III, while blue triangles indicate the simulated AOD from the best performing ensemble member (0.4Tg_BC3_13.5km_gamma5). The ensemble score is calculated from August 13, 2017 to May 31, 2018.
665
666

667
668
669
670
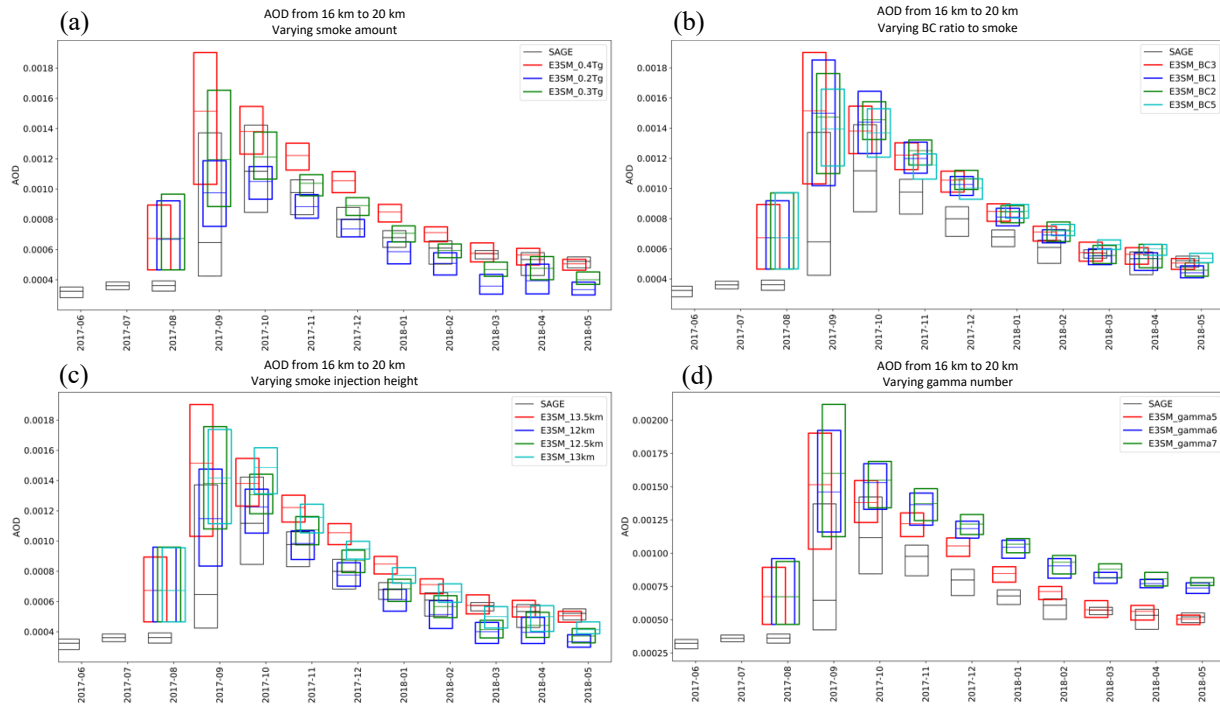
Figure 3. (a) Boxplot of daily AOD for the best performing ensemble member
(0.4Tg_BC3_13.5km_gamma5; red boxes) along with other ensemble members with varied smoke
amounts. (b) – (d) The same as (a) but varying BC ratio, injection height, and gamma number,
respectively. The black boxes show the retrieved AOD from SAGE-III. The horizontal lines of the
boxplot indicate the lower quartile, the median, and the upper quartile of daily AOD.

676
677
678
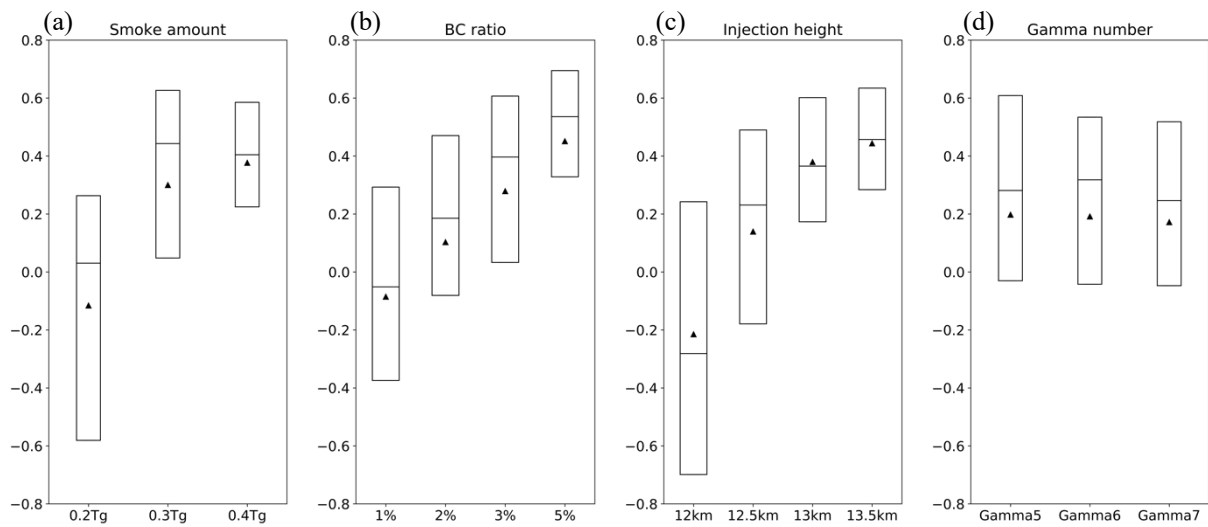
679
680 Figure 4. The boxplot and the mean of ensemble score for four perturbed parameters. The boxplot
681 displays the lower quartile, the median, and the upper quartile of ensemble score for each variable
682 number. The triangle is the mean of ensemble score for each variable number. Each ensemble
683 score is calculated from August 13, 2017 to May 31, 2018.
684
685
686
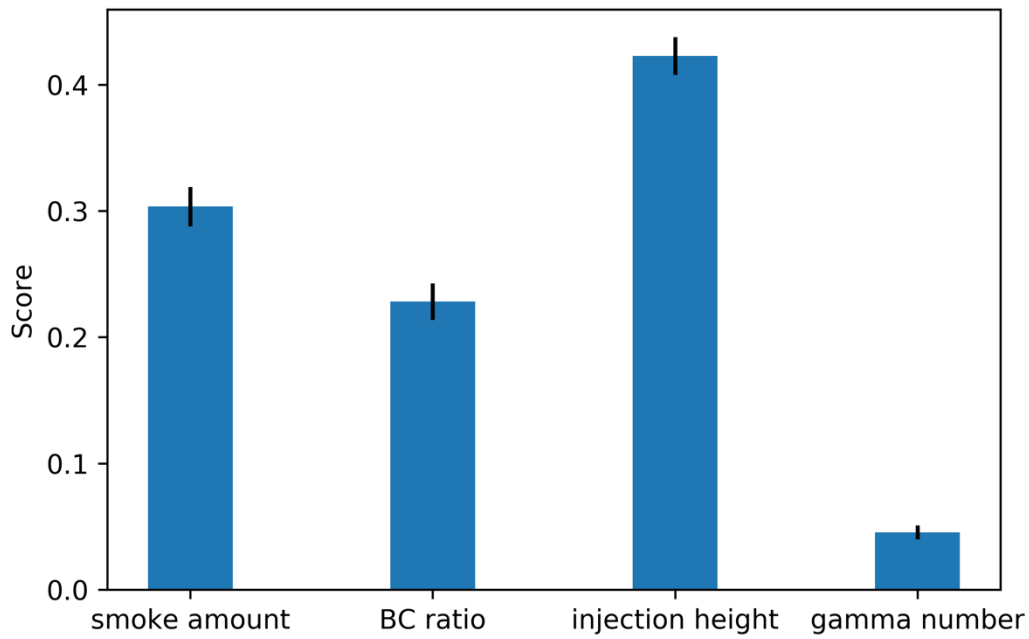
687
688 Figure 5. Feature importance calculated by the scikit-learn random forest package. Desired outputs
689 are high ensemble scores. The feature inputs are listed in Table 1. The error bar is given by the 15
690 random forest runs with different splitting of trees and training samples. The detail of the model
691 set up is presented in Section 2.5.
692

693

(a)
0.4Tg_BC3_13.5km_gamma5 Smoke sum from 16km to 20km
2017-08-14 00:00:00
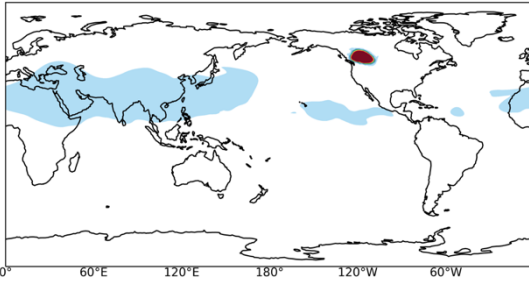
(b)
0.4Tg_BC3_13.5km_gamma5 Smoke sum from 16km to 20km
2017-08-18 00:00:00
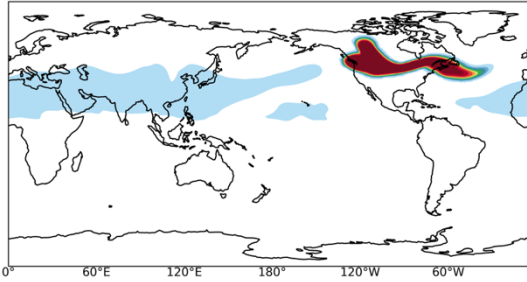
694

(c)
0.4Tg_BC3_13.5km_gamma5 Smoke sum from 16km to 20km
2017-08-21 00:00:00
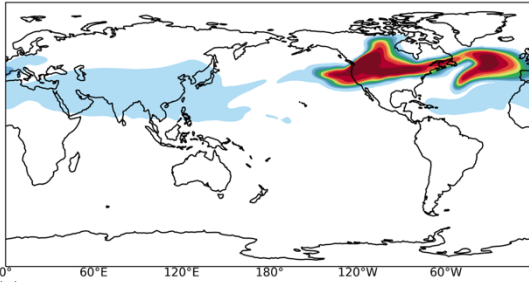
(d)
0.4Tg_BC3_13.5km_gamma5 Smoke sum from 16km to 20km
2017-08-24 00:00:00
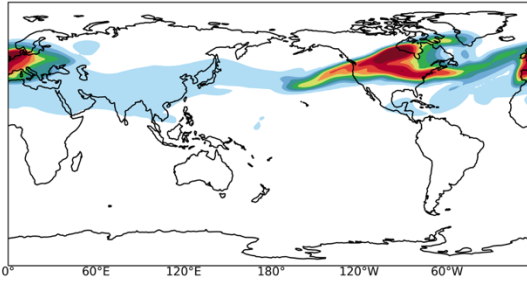
695

(e)
0.4Tg_BC3_13.5km_gamma5 Smoke sum from 16km to 20km
2017-09-01 00:00:00
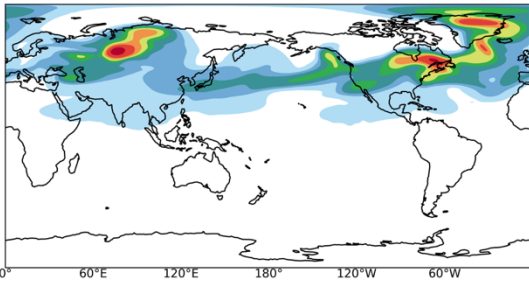
(f)
0.4Tg_BC3_13.5km_gamma5 Smoke sum from 16km to 20km
2017-09-30 00:00:00
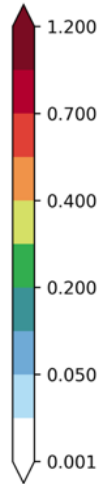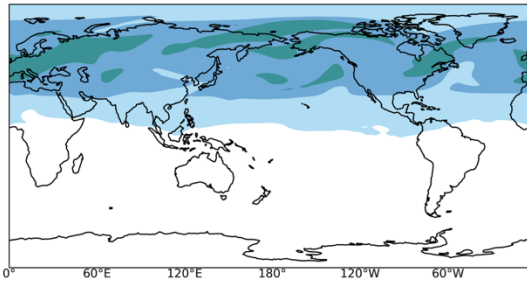
696
697 Figure 6. Integrated smoke concentration ($\times 10^{-7}$ kg m^{-2}) from 16 km to 20 km in altitude for the
698 case of 0.4Tg_BC3_13.5km_gamma5. (a) – (f) are the smoke transport on August 14, August 18,
699 August 21, August 28, September 1, and September 30, 2017, respectively.
700
701

702
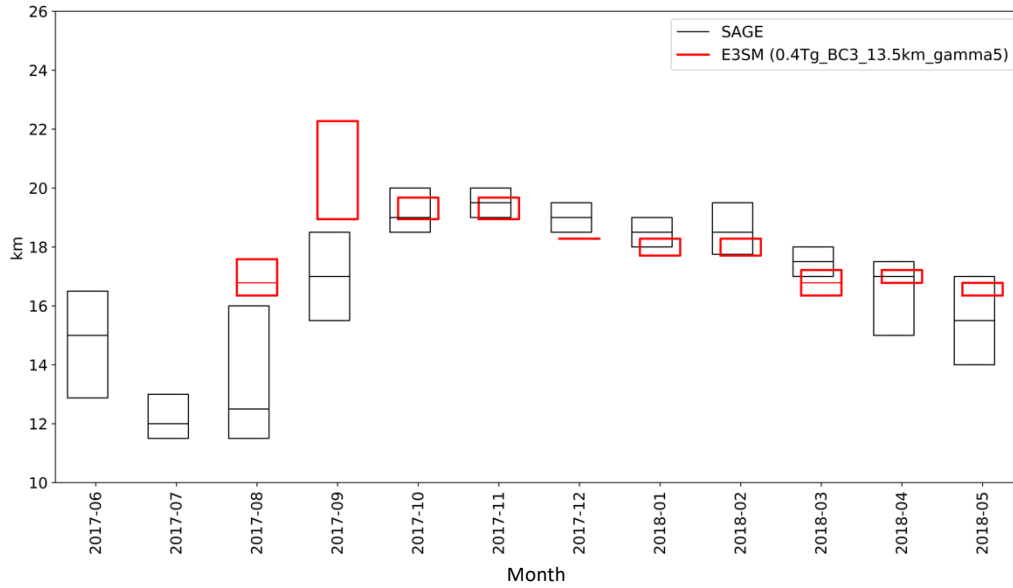
703
704
705 Figure 7. A boxplot of daily maximum plume height in 0.4Tg_BC3_13.5km_gamma5 (red boxes)
706 compared with SAGE-III observations (black boxes). Plume height is defined as the height at
707 which the aerosol extinction coefficient is greater than 1.5×10^{-4} km^{-1}. The boxplot displays the
708 lower quartile, median, and upper quartile of the daily maximum plume height.
709
710

(a)

(b)
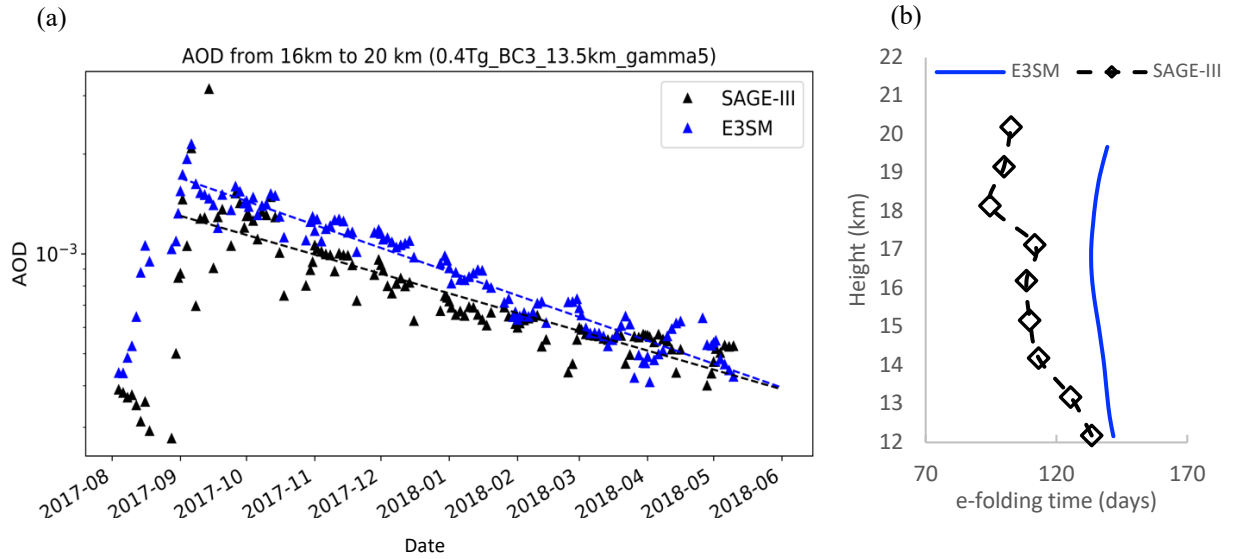
Figure 8. (a) Daily AOD as in Figure 2, but a logarithmic scale is used for the y-axis. The decay rate of E3SM AOD (blue dashed line) is calculated starting from September 1, 2017. (b) Altitude-dependent lifetime for the smoke column mass (BC+POM) concentration above each altitude in 0.4Tg_BC3_13.5km_gamma5 (blue line). Calculated smoke lifetime from SAGE-III data is the smoke column optical depth above each altitude shown by the dashed line with diamond symbols (as depicted in Yu et al. (2019)).

(a) Stratospheric smoke direct effects

	SW	LW	SW+LW
Surface	-0.292	-0.003	-0.295
Top-of-Model	0.224	-0.028	0.196
Atmosphere	0.515	-0.025	0.491

W/m²

■ Surface ■ Top-of-Model ■ Atmosphere

(b) Clear-sky net radiative effects in atmosphere (W/m²)   (c) Clear-sky net radiative effects at surface (W/m²)
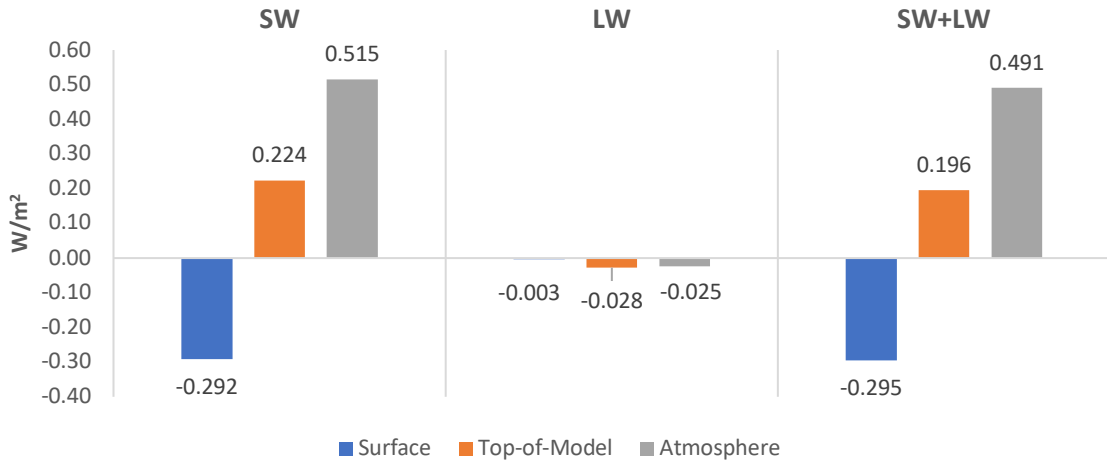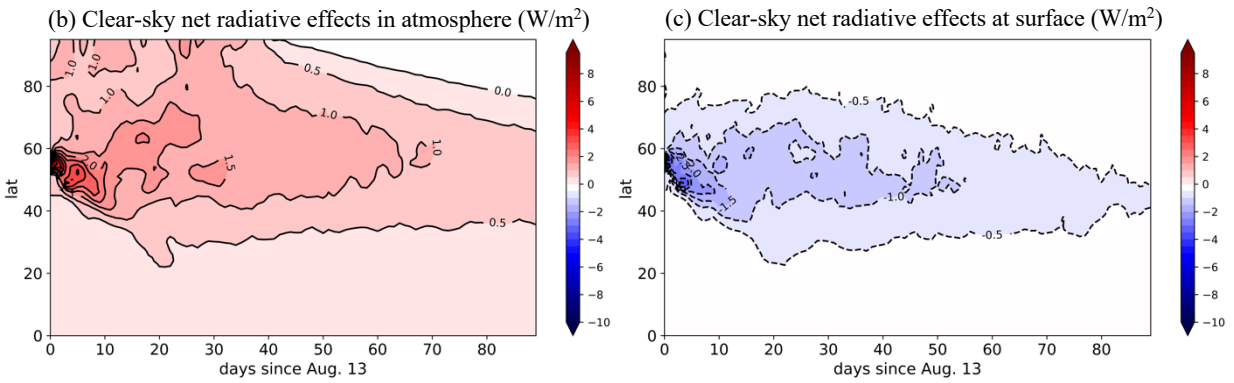
Figure 9. (a) The spatial-temporal averaged radiative effects of simulated smoke aerosols over the northern hemisphere from August 13, 2017 to May 31, 2018. (b) Time series of zonal mean clear-sky net radiative effects of smoke aerosols in atmosphere. (c) The same as (b) but at the surface. Results are from the case 0.4Tg_BC3_13.5km_gamma5.
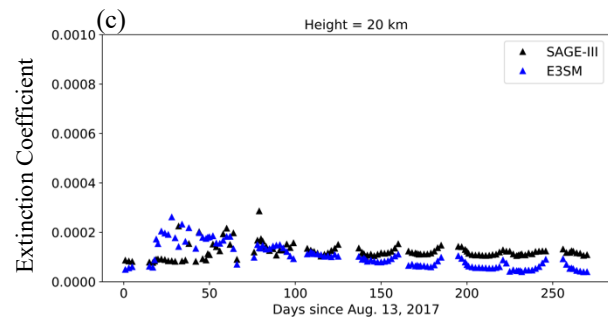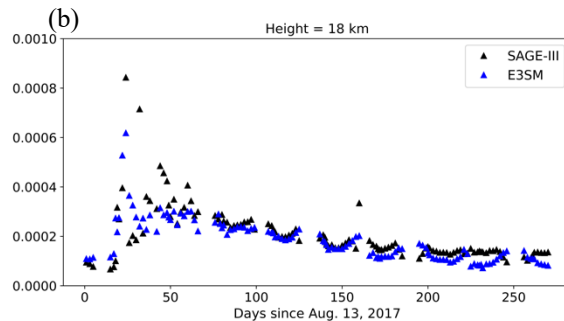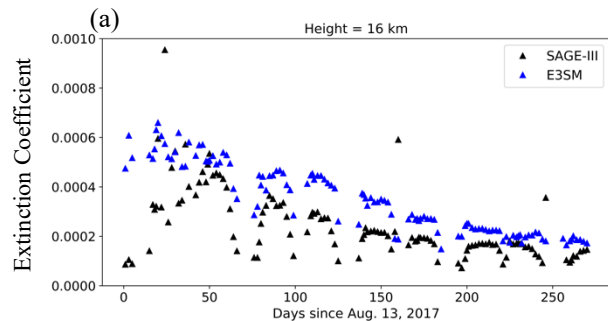
730

731
732
733 Figure 10. Time series of daily extinction coefficient (1024 nm wavelength; units: km^{-1}) at (a) 16
734 km, (b) 18 km, and (c) 20 km height. Black triangles the data from SAGE-III, while blue triangles
735 indicate the simulated extinction coefficient from 0.4Tg_BC3_13.5km_gamma5.

736